On the Accuracy and Simplifications of Battery Models using In Situ Measurements of Lithium Concentration in Operational Cells

Jason B. Siegel, Xinfan Lin and Anna Stefanopoulou

***Abstract*— In an effort to evaluate the accuracy of various battery models we use neutron imaging which is a non-destructive in situ measurement technique that has been successfully used to track the migration of lithium between the anode and cathode electrode layers during battery operation. In this work we extend the previous results, acquired during steady state conditions, by studying the transient behavior of the lithium concentration distribution across the electrode during charging and discharging. The thermal neutron beamline at the National Institute for Standards and Technology (NIST) Center for Neutron Research was used to measure the Lithium concentration in an operating Lithium Iron Phosphate (LFP) pouch cell battery with typical commercial electrodes. A stroboscopic imaging technique was developed to generate images with longer effective exposure time, increasing the signal to noise ratio and enabling measurement of changes in lithium concentration during high power transients. The measurement of the solid phase lithium concentration distribution across the electrode for high rate (7.5C / 3C) short duration (20-40s) pulses are compared with the simulated distributions from a commercial battery simulation software package using the same experimental conditions.**

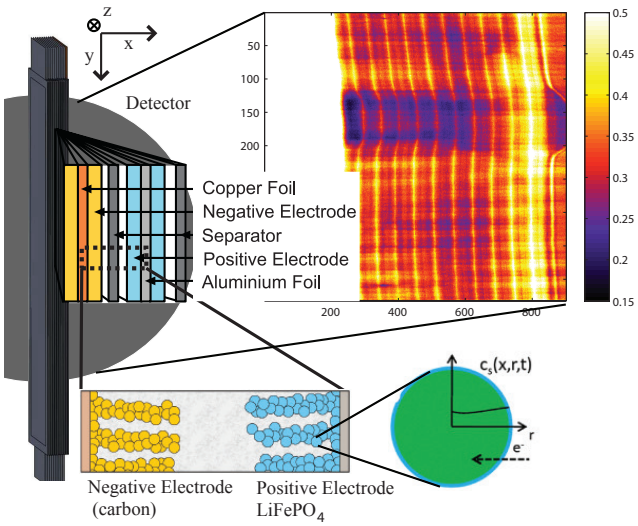

Fig. 1. Internal structure of the 10 layer stacked pouch cell battery used for neutron imaging. The neutron beam path is along the z-direction (into the page). The upper right inset image shows the relative neutron transmission image of the battery pouch cell. Each pixel in the x-direction is 5μ m wide and y-direction is 150 μm (after binning 30 pixels). The bright vertical lines correspond to the aluminum current collector (which has the lowest neutron attenuation).

J. Siegel, X. Lin, and A. Stefanopoulou are with the Department of Mechanical Engineering, University of Michigan, Ann Arbor, MI 48109, USA siegeljb@umich.edu, xflin@umich.edu, annastef@umich.edu

I. INTRODUCTION

Accurate estimates of Lithium Ion Battery State of Charge (SOC) are critical for constraining the amount of available power and energy that can be safely extracted or inserted into a battery pack. Coupled Partial Differential Equations (PDEs) describing the lithium concentration and over-potential distributions throughout the battery electrode are typically used to model the dynamics of cell voltage [1]. One of the critical limitations of Lithium ion batteries is the rate at which they can safely be charged and discharged. This limitation arises due to the minimum and maximum lithium concentrations at the interface between the solid phase and the electrolyte [2], [3], [4]. Control algorithms that account for electrolyte and solid phase lithium distributions across the electrode may better utilize the battery's stored energy and ability to meet time varying power demands while avoiding locally large over-potentials; a condition that leads to increased rate of side-reactions and lithium plating that decrease battery performance and capacity [2]. However, these PDE based models are difficult to analyze and implement in a microcontroller, therefore development of reduced order models which retain connection to the physical states are desirable. Many reduced-order models, such as the 1-D Single-Particle Model (SPM) shown in the lower right of Fig. 1, have been developed to describe Lithium transport inside the battery intercalation material. These reduced order models assume uniform or electrode-averaged behavior, and therefore may only be valid at low C-rates when the electrode reaction rate distribution is uniform. Historically validation of electrochemical battery models relied on measured terminal voltage, and this work seeks to validate the physical states (lithium concentration distribution).

Neutron Imaging (NI) is a non-destructive tool that can be used to visualize *in situ* the local change in lithium concentration across the battery electrode (x-axis) by observing the change in neutron transmission. The principle of neutron imaging is similar to x-ray radiography, where a detector is placed behind an illuminated object to measure the change in transmission through that object. Neutron interactions with the various battery materials reduce the number of transmitted neutrons. Lithium has a strong absorption cross-section for neutrons; hence the change in neutron transmission due to a change in lithium concentration can be detected. If the battery is placed so that the beam-axis (along the z-direction) is parallel to the surface of the separator as shown in Fig. 1, bisecting the anode and cathode layers of the battery, then the movement of lithium between the anode and cathode

intercalation material during charging and discharging can be observed [5].

Imaging the battery under higher-rate conditions can be used to verify up to what C-rate the SPM is valid. This presents a unique challenge for neutron imaging since the image exposure time needed to achieve less than 5% (of full scale concentration difference between charged and discharged states) measurement uncertainty (standard deviation) is greater than 10 minutes with the high-resolution neutron detector available at NIST [5]. The amount of "shot noise" and hence measurement uncertainty in the image is inversely proportional to the square root of exposure time, however increased exposure time is incompatible with our goal of imaging high-rate transient behavior. In this work we demonstrate how a stroboscopic imaging technique can be used to capture dynamic transients, while acquiring data at a faster rate, and still achieve the noise reduction benefits of time averaging. Stroboscopic imaging of periodic behavior was demonstrated in [6] by imaging a rotating computer fan. Here a periodic current excitation is applied to the battery and the start of image acquisition is synchronized with load current.

In this paper a PDE based model of the lithium distribution across the electrode is compared with neutron transmission data. First the experimental conditions are presented, then a brief discussion of the battery model. Next the image formation process is reviewed along with equations that describe how the modeled lithium concentration is related to the measurements. Finally the method of image processing and results are discussed.

II. Experimental Conditions

In this work, a high rate periodic charge and discharge pulse was applied to battery and images were taken at a fast rate ($T_{im} = 16$ s exposure time and 2 s readout) for a total data acquisition time of about 18 s. The first image from each period was averaged together to form a snapshot of the lithium distribution, corresponding to the initial portion of the pulse discharge. Similarly the images from each of the remaining 8 sequential images from the pulse cycle are averaged across multiple cycles to form a snapshot of the lithium concentration during the pulse. The periodic pulse profile, shown in Fig. 2, consisted of a 7.5 C (0.435 A) discharge for 38 s followed by a rest for 18 s and then a 3 C (0.174 A) charge for 95 s and another rest for 22 s. Two images were acquired during the discharge portion of the cycle, which extracted approximately 4.6 mAh of charge from the battery, or about 7% of the battery capacity (64 mAh). The battery SOC was near 50% at the start of the test as shown in bottom subplot of Fig. 2.

The pouch cell battery was constructed from 10 layers of double sided electrodes using standard commercial materials from A123 Systems. The electrode size was tailored for neutron imaging based the path length of the neutron beam through the material. The electrode area is 45 mm tall by 7 mm wide for the anode, and 5 mm wide for the cathode. The electrode width, δ = 5 to 7 mm was chosen to optimize both the signal to noise ratio (overall neutron transmission through the battery) and the contrast (change in neutron transmission) between the charged and discharged states. The electrodes were hand stacked on top of a Teflon spacer. The Teflon spacer was added to help maintain flatness of the battery to facilitate post processing of the images and spatial averaging. The battery consists of a porous separator placed in between each alternating anode and cathode layers. The anode layer has an offset tab protruding from the top of the battery case and the cathode layers have tabs on the opposite side (bottom) as shown in Fig. 1. Each of the tabs from the corresponding electrode was ultrasonically welded to yield a parallel electronic connection between battery layers. The $LiFePO_4$ active material is 54 μm thick applied to each side of a 20 μm aluminum current collector, for a total thickness of 127 μm for the positive electrode. The carbon active material is 39 μm thick applied to each side of a 10 μm copper current collector, yielding a total thickness of 88 μm for the negative electrode.

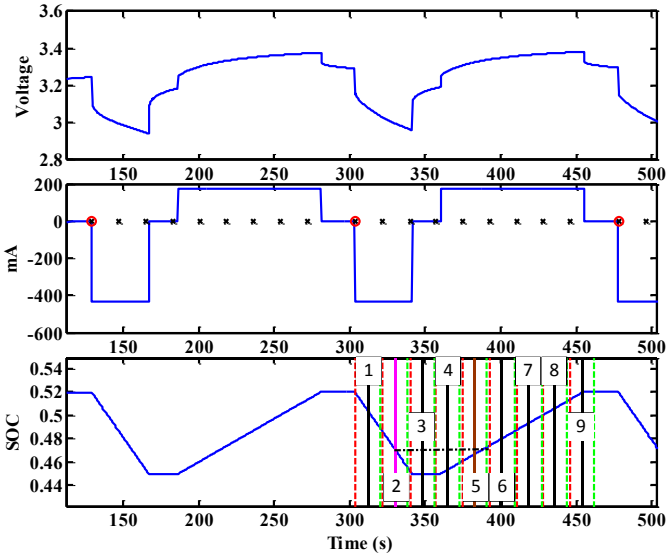

Fig. 2. Data from high-rate pulse charging and discharging of the battery around 50 percent state of charge. Two images are acquired during the discharge portion of the periodically applied current profile. Each of the nine images is summed across multiple periods to generate a snapshot of the dynamic behavior with longer effective exposure time (10 minutes). Image times are indicated by the solid vertical lines in the bottom subplot.

III. Predicted Solid Phase Li Ion Distribution across the Electrode

In order to capture the spatial distributions, the electrodes have been modeled since the early 90's as a distribution of spherical particles along the electrode [1], [7], [8], as shown in Fig. 1. Two partial differential equations (PDEs) describe the dynamics of lithium concentration distribution. The lithium concentration in the electrolyte is given by,

$$\frac{\partial}{\partial t}\left(\varepsilon_e c_e\right) = \frac{\partial}{\partial x}\left(D_e^{\text{eff}} \frac{\partial}{\partial x} c_e\right) + \frac{1 - t_+^0}{F} j^{\text{Li}} \qquad (1)$$

and in the solid phase,

$$\frac{\partial c_{\mathrm{s}}}{\partial t} = \frac{D_{\mathrm{s}}}{r^2}\frac{\partial}{\partial r}\left(r^2\frac{\partial c_{\mathrm{s}}}{\partial r}\right). \tag{2}$$

To maintain charge balance in the electrolyte and solid material the electrolyte potential (ϕ_e) and solid phase potential (ϕ_s) must also satisfy

$$\frac{\partial}{\partial x}\left(\kappa^{\mathrm{eff}}\frac{\partial}{\partial x}\phi_e\right) + \frac{\partial}{\partial x}\left(\kappa_{\mathrm{D}}^{\mathrm{eff}}\frac{\partial}{\partial x}\ln c_{\mathrm{e}}\right) + j^{\mathrm{Li}} = 0 \tag{3}$$

$$\frac{\partial}{\partial x}\left(\sigma^{\mathrm{eff}}\frac{\partial}{\partial x}\phi_{\mathrm{s}}\right) - j^{\mathrm{Li}} = 0 \tag{4}$$

The coupling between the species concentration and charge equations is described by the Butler-Volmer relation.

$$\begin{aligned} j^{\mathrm{LI}} = a_{\mathrm{s}} i_0 \Bigg\{ &\exp\left[\frac{\alpha_{\mathrm{a}}F}{RT}\left(\eta - \frac{R_{\mathrm{SEI}}}{a_{\mathrm{s}}}j^{\mathrm{LI}}\right)\right] \\ &- \exp\left[-\frac{\alpha_{\mathrm{c}}F}{RT}\left(\eta - \frac{R_{\mathrm{SEI}}}{a_{\mathrm{s}}}j^{\mathrm{LI}}\right)\right]\Bigg\} \end{aligned} \tag{5}$$

where the over-potential is given by

$$\eta = \phi_{\mathrm{s}} - \phi_{\mathrm{e}} - U \tag{6}$$

and the exchange current density is

$$i_0 = (c_{\mathrm{e}})^{\alpha_{\mathrm{a}}}(c_{\mathrm{s,max}} - c_{\mathrm{s,e}})^{\alpha_{\mathrm{a}}}(c_{\mathrm{s,e}})^{\alpha_{\mathrm{c}}}. \tag{7}$$

Various simplifications of the model can be used to reduce the computational complexity. However, care must be exercised to ensure that the model is appropriate for the simulation conditions. One common reduced order variant is the SPM, which assumes an electrode-averaged behavior [9], [10], [11]. If the applied current is low enough, then the variation in electrolyte lithium concentration across the electrode is negligible, $c_e(x,t) = c_e^{est}$ is constant, and all of the particles experience the same current density. In this case one only needs to solve the radial diffusion equation, Eq. (2), for a single particle that is representative of the entire electrode. Using NI measurements we attempt to see/verify up to what C-rate the simplified electrode average model is valid by measuring lithium concentration across the electrode.

Neutron imaging measures the average lithium concentration along the beam path. With a 13.5 μm spatial resolution of the detector, several measurements across the electrode can be achieved, but the nanometer sized particles are not resolved. Therefore, the measurement of lithium concentration in the image (across the x-direction as defined in Fig. 1) can be related to the lithium concentration in the pseudo-2D model by assuming a uniform lithium concentration along the z and y directions and averaging the lithium concentration along the radius of each spherical particle and over the image acquisition window ($T_{im} = 16\ s$).

$$\bar{c}_s(x) = \frac{3}{R_p^3}\frac{1}{T_{im}}\int_0^{R_p}\int_t^{t+T_{im}} r^2 c_s(x,r,t)\,r\,\mathrm{d}t\,\mathrm{d}r \tag{8}$$

where R_p is the radius of the spherical particle.

Simulation of the PDE model is performed using CD-Adaptco's Battery Design Studio (BDS) [12], based on the model by Fuller, Doyle, and Newman [7]. Model parameters used in the simulation will be available in an extensive publication. The particle averaged, time window averaged lithium concentration across the electrode, $\bar{c}_s(x)$, corresponding to the image acquisition times over the pulse cycle are shown in Fig. 3. The times of the third and ninth image, shown in Fig. 3, correspond to the rest periods after discharging and charging respectively. The change in lithium concentration in the positive electrode ($LiFePO_4$) shows the largest difference at the location closest to the separator. The average value of lithium concentration across the electrode is also higher in the third frame due to the lower state of charge. The change in lithium distribution between charged and discharged states across the negative electrode is much more uniform than the positive electrode. This indicates that the SPM would be a good approximation of the negative, but not the positive electrode. Images I[5] and I[6], during the charging pulse, are averaged and compared with the second image I[2] during the discharge pulse at the same nominal SOC also shown in Fig. 3. The slope difference between the charging and discharging pulses is very small, although it is larger for the positive electrode than the negative. The average value of lithium concentration across each electrode between the two cases ($I[2]$ and $(I[5]+I[6])/2$) is the same because the battery is at the same nominal SOC as calculated through coulomb counting.

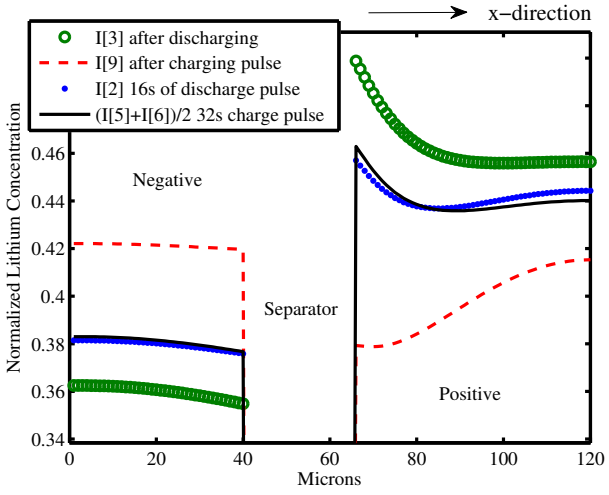

Fig. 3. Simulated average (along radius of spherical particles) of the solid intercalation material lithium concentration distribution ($\bar{c}_s(x)$). The expected maximum difference from the applied current pulse occurs between image 3 (taken after a 7.5C pulse discharge) and image 9 (after a 3C charging pulse). Image 2 and the average of images 5 and 6 have the same nominal SOC, but different lithium distribution across the electrode because of the applied current.

IV. Li Ion Concentration Metrology

Ideally we would compare the predicted lithium concentration with the observed values; however, only the change in lithium concentration from a reference image can readily be

determined from the intensity values. The image formation process introduces blurring into the image, and the data is noisy as a result of the stochastic nature of the neutron arrival process. For this reason we also model the neutron imaging process and compare the modeled neutron transmission with the measured transmission signals.

A. Principle of Neutron Imaging

The neutron beam attenuation after passing through and object of thickness δ, is described by the Lambert-Beer Law.

$$I = I_0 \exp\left(-\sigma_{Li} N_A \delta c_{Li} - N_A \delta \sum \sigma_i c_i\right) \tag{9}$$

where I_0 is the incident neutron beam intensity, σ_{Li} is the neutron cross section (cm^{-2}) of the material, N_a is Avogadro's number and c is the concentration (mol cm^{-3}). The battery fixture is mounted in front of the detector with the plane of the separator perpendicular to the surface of the detector and the battery layers are oriented along the y-axis in the detector reference frame as shown in Fig. 1.

Since the exact composition of the electrode is unknown it is not possible to use Eq. (9) to calculate the lithium concentration directly however the change in lithium concentration between images can be determined assuming the attenuation coefficient of Li, σ_{Li}, is known and that nothing else along the beam path is changing. The change in lithium concentration, between two images, is proportional to the Optical Density (OD)

$$c_{Li}(t_2) - c_{Li}(t_1) = \frac{1}{\delta N_A \sigma_{Li}} OD(t_2, t_1), \tag{10}$$

where OD is defined as,

$$OD(t_2, t_1) = -\text{Ln}\left(\frac{I(t_2)}{I(t_1)}\right). \tag{11}$$

B. Modeling the Imaging System

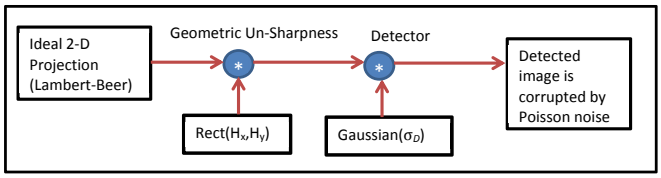

Fig. 4. Model of the Image formation process, the recorded image can be modeled as the convolution of the ideal 2-D projection image with a rectangular window and then a Gaussian.

The geometry of the imaging system and the size of the aperture impact the achievable spatial resolution. These effects have been modeled in order to compare the model with the collected images.The geometric effects of the imaging system can be modeled by convolving the ideal 2-D projection image described by the Lambert-beer law with a rectangular window of width $H_x = zD_x/L = 3.3\mu$m and $H_y = zD_y/L = 33\mu$m. The spatial resolution of the detector can be modeled by convolution with a Gaussian function with parameter $\sigma_D = 9.2$ μm. The ideal 2-D projection of the battery layer onto the detector surface can be described by Eq. (9). This ideal image is filtered by the imaging system, and corrupted by noise as shown in Fig. 4. The noise in the image which results from random nature of neutron emission and capture in the detector can be modeled as a Poisson process, with mean value λ predicted by the Lambert-Beer Law in Eq. (9) multiplied by the detector efficiency. This noise and the number of counted neutrons ultimately determine the smallest change in lithium concentration that can be detected in the image [5].

C. Image Processing

Images are first corrected for the gamma background radiation by subtracting an image taken with the local neutron beam shutter closed. The non-uniformity of gain across the detector is compensated by dividing with a flat-field image. The flat-field correction is performed on the image after binning every 4-pixels along the y-axis. Once the 4-pixel binned and flat-field corrected images have been generated, the image is stretched and shifted along the x-axis (affine transform of the x coordinate) at each y location to align the aluminum current collectors of each layer along the y-axis. This enables averaging along the y-axis. Aligning the aluminum layers in the image to those at the reference state of charge also enables correction for expansion of the material due to lithium intercalation [5]. An example of the original image is shown in Fig. 1. In this radiographic image the battery structure is clearly visible. The 10 bright vertical lines correspond to the aluminum current collector, which has very low neutron attention relative to the other material used in the battery. The battery was mounted into a spring loaded aluminum fixture and a rubber strip visible on the right side of the image, Fig. 1, was used to apply even pressure (5 psi) across the active area during cycling of the pouch cell. The rubber is a strongly scattering material and caused the apparent higher neutron transmission in the two adjacent battery layers. The increased neutron count in this region is constant over time and therefore does not impact the quantification of changes in lithium concentration.

Once the images are aligned the line profile across the x-direction is formed by averaging along the entire y-axis, (approximately 4000 pixels or 2 cm in the original image) as shown in the upper subplot of Fig. 5. The 4000 pixel spatial average yields the same improvement in image noise reduction as increasing the exposure time by a factor of 4000. On average about 4 neutrons per pixel per minute are detected with an open beam, due to the small pixel size ($\Delta = 5\mu$ m), thus necessitating long exposure time and spatial averaging to achieve a good signal to noise ratio.

V. Results

The line profile data corresponding to the relative transmission through the battery at 100% state of charge in steady state (Reference image) and 50% SOC during the second half of the pulse discharge are shown in the upper subplot of Fig. 5. This data is first presented to illustrate the magnitude of change in neutron transmission corresponding to 50% change in SOC and the challenge of quantifying small

changes in Li concentration gradient across the electrode due to blurring and noise effects in the image. The lower subplot of Fig. 5 shows the optical density, which is proportional to the change in lithium concentration between the two images. The negative electrode is delithiated during a discharge, which leads to the negative OD in this region (highlighted in orange). The optical density corresponding to a difference of 50% SOC is about 0.03 ± 0.005 for the positive electrode and -0.04 ± 0.005 for the negative electrode.

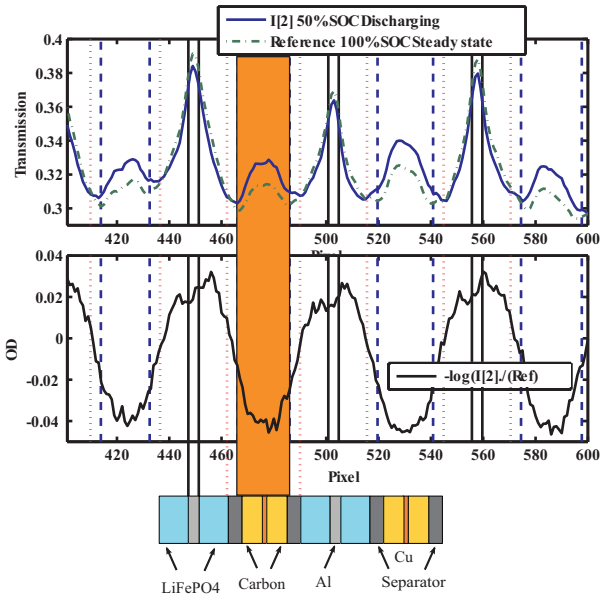

Fig. 5. Upper subplot shows the relative neutron transmission data in the charged state, and during the 2nd half of the pulse discharge corresponding to image I[2]. The negative electrode is delithiated during discharge, which leads to negative OD in this region (highlighted in orange).

A. Experimental Line Profile Data

Figure 6(a) shows the line profile data for neutron transmission and optical density for the times of the third (I[3]) and ninth image (I[9]). These times correspond to the rest periods (zero applied current) after discharging and charging respectively. A small change in neutron transmission can be observed in the upper subplot due to a 7% average change in lithium concentration. The optical density, shown in the lower subplot, is proportional to the local change in lithium concentration, and here is attributed to the bulk SOC difference. The optical density in Fig. 6(a) shows a larger overall change in lithium concentration, as compared to Fig. 6(b) which corresponds to the same bulk SOC but different current direction.

In order to investigate the change in lithium distribution across the electrode during high-rate charging and discharging, two line profiles with the same nominal state of charge (and hence same average lithium concentration) are compared in Fig. 6(b). The first transmission line profile, shown in the upper subplot, corresponds to the second image in the sequence $I[2]$ taken from the 2nd half of the pulse discharge. This data is compared with the average of the first two images from the charging pulse, images five and six ($(I[5]+I[6])/2$). The average of these two images has the same nominal SOC as $I[2]$. The change in neutron transmission between the two cases is virtually indistinguishable to the naked eye; however, the optical density in the lower subplot shows a change in lithium concentration which is greater than the noise level indicating a difference in the lithium concentration profile across the electrode between charging and discharging pulses. So our experiments verify that the electrode average assumption does not hold for this high pulse current rate.

B. Comparison with Simulated of Line Profiles

A simulation of the neutron image formation process can be used to compare the output of a commercial battery electrode solver (BDS) with the neutron imaging data. The simulation of the lithium concentration across the electrode is shown in Fig. 3 for the four cases outlined above from the discharging and charging profile. The simulated ideal and blurred optical density line profiles are shown in Fig. 6(c) and Fig. 6(d). The difference in lithium concentration across the positive electrode is more pronounced in the region nearest the separator, however this feature is difficult to identify in the blurred optical density. The difference in slope between the charged (I[3]) and discharged (I[9]) line profiles is much less than the bulk change in lithium between these times. This can be seen in Fig. 6(c) by noticing that the optical density does not cross zero (change sign) within region corresponding to either electrode. This however is not the case for the other pair of images, which have the same nominal SOC, shown in Fig. 6(d). Finally notice the shape of the simulated optical density is different between the two cases, Fig. 6(c) and Fig. 6(d). The dual peaks in the simulated line profile of the positive electrode in Fig. 6(c), corresponding to a dip caused by the aluminum layer, are faintly visible in the experimental data Fig. 6(a).

VI. CONCLUSIONS AND FUTURE WORK

Despite the small change in Li concentration predicted by the numerical simulation for the periodic pulsed current profile, the Neutron Imaging is capable of distinguishing the changes in spatial distribution of lithium across the electrode. The blurring and noise present in the images may obscure the features of the Li-concentration profile predicted by the simulation however a difference in the slope of the distribution can still be detected in the data for the latter pair of images, which have the same average concentration but different applied current, suggesting that the electrode average model would not be a suitable choice for this high C-rate. Evaluation of the impact of changes in electrolyte lithium concentration distribution between charging and discharging on the measurement will be investigated in future work. It is suspected that change in electrolyte lithium concentration may be large relative to the change in solid phase lithium concentration for the short duration pulses at high C-rate between I[2] and (I[5]+I[6])/2. In order to better utilize

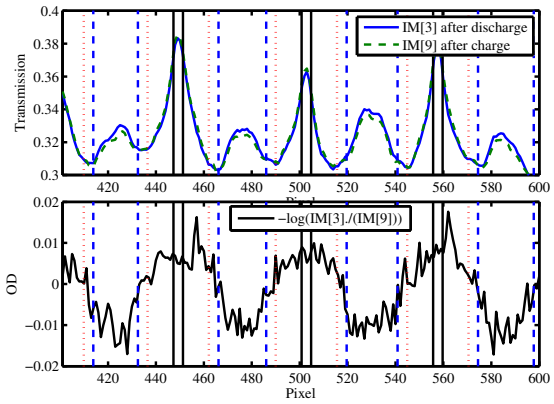

(a) Difference in Lithium concentration between ($I[9]$) following a 3C charge for 95 s and ($I[3]$) after 7.5C discharge for 38 s (charge concentration minus discharge). Notice that the cathode exhibits the largest deviation in local Lithium concentration.

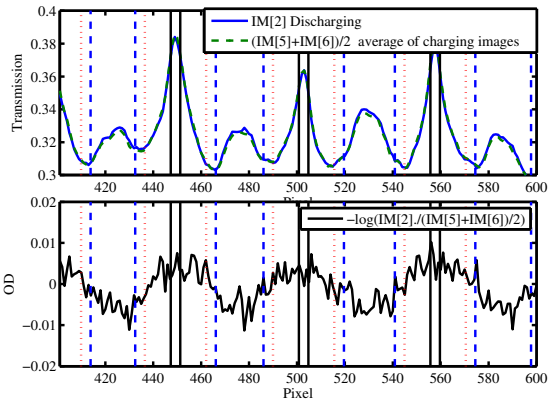

(b) Difference in Lithium concentration between the second image $I[2]$ during discharge, and $(I[5] + I[6])/2$ during charging at same nominal SOC, but at a lower C rate. Some difference between local lithium concentrations across the electrode is evident by the non-zero optical density.

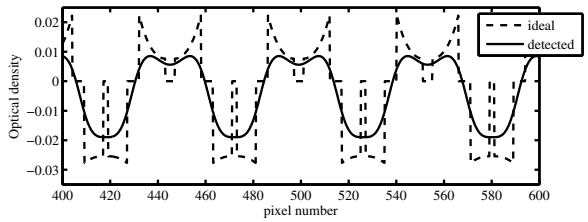

(c) Simulated Optical Density line profile for modeled Li concentration during rest periods with maximal difference in SOC (same conditions as Fig. 6(a)). $I[3]$ vs $I[9]$.

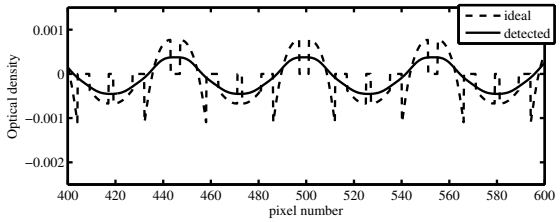

(d) Simulated Optical Density line profile for pulse data during charge and discharge (same conditions as Fig. 6(b)). $I[2]$ vs $(I[5] + I[6])/2$.

Fig. 6. Comparison between the neutron imaging data and the simulated line profiles (using the lithium concentration from BDS).

this type of measurement there is a need to address the challenging inverse problem of how to extract and calibrate a distributed parameter model from noisy blurred image data. This work details the necessary modeling framework which is a critical first step to accomplish this task. In order to overcome the current limitation of detector spatial resolution future experiments are planned using thicker electrodes and longer exposure time to measure the concentration gradient across the electrode with better fidelity.

VII. ACKNOWLEDGMENTS

The authors would like to thank the instrument scientists Daniel Hussey and David Jacobson at NIST, David Gorsich and Yi Ding from TARDEC, and Danny King and Patrick Hagans from A123 Systems for help constructing a pouch cell with electrode area that was optimized for imaging.

REFERENCES

[1] M. Doyle, T. F. Fuller, and J. Newman, "Modeling of galvanostatic charge and discharge of the lithium/polymer/insertion cell," *J. Electrochem. Soc.*, vol. 140, no. 6, pp. 1526–1533, Jun. 1993.

[2] K. Smith, C. Rahn, and C.-Y. Wang, "Model-based electrochemical estimation and constraint management for pulse operation of lithium ion batteries," *IEEE Transactions on Control Systems Technology*, vol. 18, no. 3, pp. 654–663, 2010.

[3] Y. Zhang, C.-Y. Wang, and X. Tang, "Cycling degradation of an automotive lifepo4 lithium-ion battery," *Journal of Power Sources*, vol. 196, no. 3, pp. 1513–1520, Feb. 2011.

[4] D. D. Domenico, A. Stefanopoulou, and G. Fiengo, "Lithium-ion battery state of charge and critical surface charge estimation using an electrochemical model-based extended kalman filter," *Journal of Dynamic Systems, Measurement, and Control*, vol. 132, p. 061302 (11 pages), 2010.

[5] J. B. Siegel, X. Lin, A. G. Stefanopoulou, D. S. Hussey, D. L. Jacobson, and D. Gorsich, "Neutron imaging of lithium concentration in lfp pouch cell battery," *J. Electrochem. Soc.*, vol. 158, no. 5, pp. A523–A529, May 2011.

[6] A. Tremsin, M. Muhlbauer, B. Schillinger, J. McPhate, J. Vallerga, O. Siegmund, and W. Feller, "High resolution stroboscopic neutron radiography at the frm-ii antares facility," *IEEE Transactions on Nuclear Science*, vol. 57, no. 5, pp. 2955–2962, 2010.

[7] T. F. Fuller, M. Doyle, and J. Newman, "Simulation and optimization of the dual lithium ion insertion cell," *J. Electrochem. Soc.*, vol. 141, no. 1, pp. 1–10, Jan. 1994.

[8] K. A. Smith, "Electrochemical control of lithium-ion batteries [applications of control]," *IEEE Control Systems*, vol. 30, no. 2, pp. 18–25, 2010.

[9] K. Smith and C.-Y. Wang, "Solid-state diffusion limitations on pulse operation of a lithium ion cell for hybrid electric vehicles," *Journal of Power Sources*, vol. 161, no. 1, pp. 628–639, Oct. 2006.

[10] S. Santhanagopalan, Q. Guo, P. Ramadass, and R. E. White, "Review of models for predicting the cycling performance of lithium ion batteries," *Journal of Power Sources*, vol. 156, no. 2, pp. 620 – 628, 2006.

[11] C. Speltino, D. Di Domenico, G. Fiengo, and A. Stefanopoulou, "Comparison of reduced order lithium-ion battery models for control applications," in *Proceedings of the 48th IEEE Conference on Decision and Control, 2009 CDC/CCC 2009.*, dec. 2009, pp. 3276 –3281.

[12] *Battery Design Studio*. [Online]. Available: http://www.cd-adapco.com/products/battery_design_studio/index.html